The Astrophysical Journal Supplement Series, 270:29 (28pp), 2024 February https://doi.org/10.3847/1538-4365/ad12c1

Evolution and Final Fate of Solar Metallicity Stars in the Mass Range 7–15 $M_\odot$. I. The Transition from Asymptotic Giant Branch to Super-AGB Stars, Electron Capture, and Core-collapse Supernova Progenitors

Marco Limongi[1,2,3], Lorenzo Roberti[1,4,5], Alessandro Chieffi[3,6,7], and Ken'ichi Nomoto[2]
[1] Istituto Nazionale di Astrofisica—Osservatorio Astronomico di Roma, Via Frascati 33, I-00040, Monteporzio Catone, Italy; marco.limongi@inaf.it
[2] Kavli Institute for the Physics and Mathematics of the Universe (WPI), The University of Tokyo Institutes for Advanced Study, The University of Tokyo, Kashiwa, Chiba 277-8583, Japan
[3] INFN, Sezione di Perugia, via A. Pascoli s/n, I-06125 Perugia, Italy
[4] Konkoly Observatory, Research Centre for Astronomy and Earth Sciences, Eötvös Loránd Research Network (ELKH), Konkoly Thege Miklós út 15-17, H-1121 Budapest, Hungary
[5] CSFK, MTA Centre of Excellence, Budapest, Konkoly Thege Miklós út 15-17, H-1121, Hungary
[6] Istituto Nazionale di Astrofisica—Istituto di Astrofisica e Planetologia Spaziali, Via Fosso del Cavaliere 100, I-00133, Roma, Italy
[7] Monash Centre for Astrophysics (MoCA), School of Mathematical Sciences, Monash University, VIC 3800, Australia
Received 2023 October 30; revised 2023 November 17; accepted 2023 November 27; published 2024 January 30

Abstract

According to a standard initial mass function, stars in the range 7–12 $M_\odot$ constitute ∼50% (by number) of the stars more massive than ∼7 $M_\odot$, but in spite of this, their evolutionary properties, and in particular their final fate, are still scarcely studied. In this paper, we present a detailed study of the evolutionary properties of solar metallicity nonrotating stars in the range 7–15 $M_\odot$, from the pre-main-sequence phase up to the presupernova stage or an advanced stage of the thermally pulsing phase, depending on the initial mass. We find that (1) the 7.00 $M_\odot$ star develops a degenerate CO core and evolves as a classical asymptotic giant branch (AGB) star in the sense that it does not ignite the C-burning reactions, (2) stars with initial mass $M \geqslant 9.22\,M_\odot$ end their lives as core-collapse supernovae, (3) stars in the range $7.50 \leqslant M/M_\odot \leqslant 9.20$ develop a degenerate ONeMg core and evolve through the thermally pulsing super-AGB phase, (4) stars in the mass range $7.50 \leqslant M/M_\odot \leqslant 8.00$ end their lives as hybrid CO/ONeMg or ONeMg WDs, and (5) stars with initial mass in the range $8.50 \leqslant M/M_\odot \leqslant 9.20$ may potentially explode as electron-capture supernovae.

Unified Astronomy Thesaurus concepts: Stellar evolutionary models (2046); Late stellar evolution (911); Stellar evolution (1599); Supernovae (1668); Core-collapse supernovae (304); Asymptotic giant branch stars (2100); Massive stars (732)

Supporting material: machine-readable table

1. Introduction

In the general picture of stellar evolution, stars with $M \lesssim 7\,M_\odot$ evolve along the thermally pulsing asymptotic giant branch (TP-AGB) phase and end their lives as CO white dwarfs (CO WDs). On the contrary, stars with $\gtrsim 12\,M_\odot$, the so-called massive stars (MSs), evolve through all of the major stable nuclear burning stages and eventually explode as core-collapse supernovae (CCSNe) leaving a compact remnant, i.e., either a neutron star or a black hole. Stars between ∼7 and ∼12 $M_\odot$ have a much more complex evolution. The lower masses ignite C off-center in an electron-degenerate environment, and their ability to remove the degeneracy totally relies on the capability of the thermally unstable zones (the convective zones) to heat the layers below the main burning front. The higher masses, on the contrary, ignite C burning centrally. After the C-burning phase, the lower-mass stars ($M \lesssim 10\,M_\odot$) develop an inert ONeMg electron-degenerate core and enter the TP phase along the AGB. These stars are generally referred to as super-AGB (SAGB) stars. The final fate of the SAGBs depends on the competition between the core growth and the mass loss (Nomoto 1984). If mass loss dominates, the envelope is completely lost, and the result is an ONeMg WD. On the contrary, if the core grows in mass enough to achieve central densities close to the threshold density for electron capture (EC) ^{20}Ne(e$^-$, ν)^{20}Fe, deleptonization and thermonuclear instability develop to induce the electron-capture supernova (ECSN). The final fate of such stars depends on the competition between the energy released by the nuclear burning front and the loss of pressure due to the deleptonization occurring in the central zones. If the energy released by nuclear burning prevails, degeneracy is removed, and the star explodes as a thermonuclear ECSN (Miyaji et al. 1980; Isern et al. 1991; Nomoto & Kondo 1991; Jones et al. 2016; Nomoto & Leung 2017). If, on the contrary, the deleptonization dominates, the collapse cannot be halted, and the star collapses into a neutron star (core-collapse ECSN; Miyaji et al. 1980; Miyaji & Nomoto 1987; Nomoto 1987; Kitaura et al. 2006; Fischer et al. 2010; Jones et al. 2016; Radice et al. 2017; Zha et al. 2019, 2022). Which outcome is realized from ECSNe depends on the details of the modeling of both the presupernova evolution and the explosion.

Stars in the mass range ∼10–12 $M_\odot$ ignite Ne burning off-center that develops in a similar fashion as the off-center C burning (Nomoto 1984). The final fate of these stars depends, once again, on the behavior of the off-center Ne burning (Nomoto & Hashimoto 1988). If the Ne burning is ignited far enough off-center, the contracting core may achieve densities

sufficiently high for the URCA processes to be activated until the conditions for an ECSN are reached before the Ne burning front is able to reach the center. If, on the contrary, the Ne burning front reaches the center before the activation of the URCA processes, O burning first and Si burning later are ignited off-center, ultimately leading to a CCSN (Jones et al. 2013, 2014; Nomoto 2014; Woosley & Heger 2015).

Stars in the range 7–12 $M_{\odot}$ constitute roughly 50% of the stars (by number) more massive than $\sim$7 $M_{\odot}$ according to a standard initial mass function (IMF). This means that proper knowledge of how they evolve and die is crucial for many astrophysical subjects. Determining the mass boundaries between stars that form CO WDs, ONeMg WDs, ECSNe, and CCSNe is mandatory to understand the relative frequencies among these objects. If a substantial fraction of stars does indeed explode as ECSNe, then they may contribute significantly to the overall SN rate and also to the population of neutron stars. ECSNe have also been proposed as potential sites for the *r*-process (Ning et al. 2007), which is responsible for the synthesis of roughly half of the nuclei above the Fe group. The ECSN has been proposed for SN 1054, which formed the Crab Nebula, in consideration of the similarity of low explosion energies and the small amount of heavy elements between the Crab Nebula and the ejecta of the ECSN (Nomoto et al. 1982). ECSNe may explain the observations of subluminous type II plateau supernovae (SNIIP) with a low amount of ^{56}Ni ejected (Smartt 2009). Recently, Hiramatsu et al. (2021) observed SN II 2018zd and found that its several observed features can be well explained by an ECSN but not by an Fe-CCSN. In the context of the chemical evolution of the galaxies, because of the shape of the IMF, these stars should contribute significantly to the production of some specific isotopes. Also, the chemical yields produced by stars in this mass interval are either completely ignored or obtained by means of an arbitrary interpolation between the yields produced by the AGB stars and those produced by the MS. In both cases, a significant error can be made. Moreover, a large fraction of MSs are part of binary or multiple systems (Duchêne & Kraus 2013). Binary interactions crucially affect the amount of mass lost by these stars, and hence even more massive progenitors may contribute to produce ECSNe (see, e.g., Brinkman et al. 2023, and references therein). Unfortunately, the binary scenario remains mostly unexplored so far.

Despite their astrophysical relevance, not many models in the range 7–12 $M_{\odot}$ that cover the full evolution are available at present. In particular, none of the papers found in the literature on this subject (e.g., Ritossa et al. 1999; Siess 2010; Ventura et al. 2011; Karakas et al. 2012; Lau et al. 2012; Gil-Pons et al. 2013; Jones et al. 2013, 2014; Takahashi et al. 2013, 2019; Ventura et al. 2013; Doherty et al. 2015; Woosley & Heger 2015; Zha et al. 2019) present a homogeneous, detailed, and comprehensive study of the full evolution of stars in the mass range 7–12 $M_{\odot}$, with a rather fine mass grid. In some cases, as has been reported in a number of recent papers, the TP phase cannot be followed due to numerical problems, and the core growth is treated parametrically, assuming an arbitrary accretion rate, or even neglected (Woosley & Heger 2015; Takahashi et al. 2019). Moreover, the full evolution of these stars with rotation has never been computed, as far as we know. The main reason for the paucity of models in this mass range is that the computation of their evolution is extremely challenging from a numerical point of view, and in general, it also requires an enormous amount of computer time and memory. As already mentioned above, in these stars, depending on the initial mass, C, Ne, O, and Si burning ignite off-center, and the burning front propagates inward in mass accompanied by a number of convective shells. A proper treatment of the heat transfer from the burning front to the underlying layers requires an extremely fine spatial resolution of the order of a few kilometers. The full coupling of convective mixing and nuclear burning, possibly coupled to the structure equations, is also necessary to properly follow these stages and avoid numerical instabilities. The adoption of a quite extended nuclear network, including at least 100 or more nuclear species fully coupled to the stellar evolution, is also needed to properly compute the energy generation and trace the abundance of the various isotopes, in particular the electron fraction. A very large number of thermal pulses is expected for SAGB stars, ranging from several tens to thousands. Typically, the thickness of the intershell region, i.e., between the He and H shells, is of the order of 10^{-4}–10^{-5} $M_{\odot}$. Resolving all of these phenomena, both in space and in time, is extremely challenging and generally requires several thousands of zones per model and hundreds of thousands, if not millions, of models to cover the entire evolution. Coupling an extended network to these kinds of models implies the need for an enormous amount of computing time to calculate a full single evolution.

This is the first paper of a series in which we aim to study in detail the evolutionary properties of stars in the transition from AGB stars to CCSN progenitors and how they change with initial metallicity and rotation velocity. In this paper, we present the detailed evolution of solar metallicity nonrotating stars in the range 7–15 $M_{\odot}$ from the pre-main-sequence phase up to the presupernova stage or an advanced stage of the TP phase, depending on the initial mass. The main goals are to (1) study how the evolutionary properties of these stars change in the transition from AGBs to MSs, (2) determine the limiting masses between AGB and SAGB stars and between SAGB stars and MSs, (3) determine their final fate, and ultimately, (4) identify the limiting masses that mark the transitions from the various final outcomes, i.e., CO WDs, ONe WDs, ECSNe, and CCSNe.

2. Stellar Evolution Code and Nuclear Network

In the last 20 yr, we have developed and continuously improved upon our stellar evolution code FRANEC (Chieffi & Limongi 2013; Limongi & Chieffi 2018). One of the strengths of the code is that it can automatically manage nuclear networks, including an arbitrarily extended list of isotopes and associated reactions. Another feature that makes this code unique in the panorama of the stellar evolution codes is that all of the equations describing (a) the physical structure of the star, (b) the chemical evolution due to the nuclear reactions, and (c) the chemical mixing due to a variety of instabilities (thermal and mechanical) are coupled together in a single system of equations and solved simultaneously. Last, but not least, FRANEC includes the treatment of the stellar rotation, the transport of the angular momentum, and the rotation-induced mixing of the chemicals. The multithreads/parallel solver algorithms used to invert the large sparse matrices needed to solve the system of equations are the most sophisticated and fastest presently available. All of the features mentioned above make this code extremely robust and fast from a numerical point of view and suitable to study essentially all of the

evolutionary phases of stars, even the most challenging ones, like the advanced burning stages of MSs; the off-center C, Ne, O, and Si burning; and the thermal pulses in AGB and SAGB stars.

All of the models presented in this paper have been computed by means of the latest version of the FRANEC code. This version is essentially the one adopted in Chieffi & Limongi (2013) and Limongi & Chieffi (2018), with the following updates/differences.

The induced overshooting occurring during the core He-burning phase, because of the transformation of He into C and O, is properly taken into account following Castellani et al. (1985). During the late stages of core He burning, the occurrence of the breathing pulses has been properly inhibited as described in Caputo et al. (1989) and Chieffi & Straniero (1989).

The equation of state adopted is the one provided by F. X. Timmes and is available on his web page.[8] It takes into account all stages of Saha ionization, plus a simple density ionization model, for elements between H and Zn for all degrees of degeneracy and relativity. In addition to that, electron positron pairs and Coulomb corrections are also taken into account.

Since in this work, we are mainly interested in studying the physical properties of the stars in the transition between AGB and MSs, and since the calculation of these models requires an enormous amount of computer time and memory, we have chosen a nuclear network that includes the minimum number of isotopes but at the same time guarantees the calculation of the nuclear energy with great accuracy. The 112 isotopes included in the adopted network are reported in Table 1. All of these isotopes are coupled among each other by the most efficient reactions due to the weak and strong interactions, for a total of about 466 reactions. Among them, we have also taken into account the following 20 URCA processes, due to their crucial role played in some of the models presented in this work:

$$^{27}\mathrm{Al}(e^-,\nu)^{27}\mathrm{Mg}(e^-,\nu)^{27}\mathrm{Na}$$
$$^{27}\mathrm{Na}(\beta^-,\bar{\nu})^{27}\mathrm{Mg}(\beta^-,\bar{\nu})^{27}\mathrm{Al}$$
$$^{25}\mathrm{Mg}(e^-,\nu)^{25}\mathrm{Na}(e^-,\nu)^{25}\mathrm{Ne}$$
$$^{25}\mathrm{Ne}(\beta^-,\bar{\nu})^{25}\mathrm{Na}(\beta^-,\bar{\nu})^{25}\mathrm{Mg}$$
$$^{23}\mathrm{Na}(e^-,\nu)^{23}\mathrm{Ne}(e^-,\nu)^{23}\mathrm{F}$$
$$^{23}\mathrm{F}(\beta^-,\bar{\nu})^{23}\mathrm{Ne}(\beta^-,\bar{\nu})^{23}\mathrm{Na}$$
$$^{24}\mathrm{Mg}(e^-,\nu)^{24}\mathrm{Na}(e^-,\nu)^{24}\mathrm{Ne}$$
$$^{24}\mathrm{Ne}(\beta^-,\bar{\nu})^{24}\mathrm{Na}(\beta^-,\bar{\nu})^{24}\mathrm{Mg}$$
$$^{20}\mathrm{Ne}(e^-,\nu)^{20}\mathrm{F}(e^-,\nu)^{20}\mathrm{O}$$
$$^{20}\mathrm{O}(\beta^-,\bar{\nu})^{20}\mathrm{F}(\beta^-,\bar{\nu})^{20}\mathrm{Ne}.$$

The energy release/absorption associated with these reactions has been treated as described in Miyaji et al. (1980).

The nuclear cross sections have been updated by taking into account the most recent experimental data and theoretical calculations, as described in Roberti et al. (2024). In particular, since the URCA rates must be carefully calculated (Toki et al. 2013; Nomoto & Leung 2017), we have adopted for these processes the refined EC and beta decay rates provided by Suzuki et al. (2016).

[8] https://cococubed.com

Table 1
Nuclear Network Adopted in the Present Calculations

Element	$A_{\min}$	$A_{\max}$	Element	$A_{\min}$	$A_{\max}$
H	1	3	P	29	33
He	3	4	S	31	35
Li	7	7	Cl	33	37
Be	7	7	Ar	36	38
C	12	13	K	39	39
N	13	15	Ca	40	44
O	15	20	Sc	43	45
F	17	23	Ti	44	50
Ne	20	25	V	47	51
Na	23	27	Cr	48	54
Mg	24	27	Mn	51	55
Al	26	27	Fe	52	58
Si	28	30	Co	55	59
			Ni	56	60

The zones unstable for convection are determined according to the Ledoux criterion in the H-rich layers and according to the Schwarzschild criterion in all of the other cases. As is well known, convective core overshooting during core H burning determines the size of the He core at core H depletion that, in turn, drives all of the following evolution of the star (Bressan et al. 1981; Bertelli et al. 1986; Temaj et al. 2013), unless the He core is further reduced by the mass loss during core He burning (Limongi & Chieffi 2006; Chieffi & Limongi 2013). In the present version of the code, we use the same prescription used in the previous version adopted in Limongi & Chieffi (2018); i.e., during core H burning, we assume $0.2\,H_P$ of convective core overshooting by computing $H_P = (P/\rho g)$ at the outer edge of the formal convective core, defined by the stability criterion mentioned above. Some amount of extra mixing is assumed at the lower edge of the convective envelope and the convective shells that form within the electron-degenerate CO core and that are associated with C, NeO, and Si off-center nuclear burning. The mixing efficiency in these zones is determined by assuming an exponentially decaying convective velocity given by

$$v_{\rm conv}(r) = v_{\rm conv}(r_0)\exp\left(-\frac{r_0 - r}{f H_P(r_0)}\right),$$

where the subscript 0 refers to values corresponding to the lower border of the convective zone, $v_{\rm conv}(r_0)$ is computed in the context of the mixing-length theory, and the free parameter f is assumed equal to 0.014. The diffusion coefficient is then computed as

$$D(r) = \frac{1}{3} v_{\rm conv}(r) H_P(r).$$

When a fuel is ignited off-center, because of the temperature inversion due to the degeneracy of the matter (see, e.g., Figures 1–3 in Nomoto 1984), a convective shell develops, and a sharp discontinuity in the temperature forms at the base of the convective zone, where burning is occurring. The capability of the burning front to propagate inward in mass, i.e., as a continuous flame or by recurrent flashes, as well as its speed, is in general controlled by the coupling of convective mixing and heat transfer from the hot zones at the base of the convective shell, where burning is occurring, to the radiative cooler and

inert zones beneath. Generally speaking, if the heat transfer is efficient enough, one expects a burning front continuously propagating toward progressively more internal zones. On the contrary, if the heat transfer is not efficient enough, the propagation of the burning front toward the center, e.g., ONe burning, has been found to occur by compressional heating (Figures 26 and 27 in Nomoto & Hashimoto 1988) through a sequence of convective shells that form where the fuel is abundant and disappears as the fuel is locally exhausted. The treatment of such a phenomenon is not trivial, and different approaches and assumptions can be followed (see, e.g., Nomoto & Hashimoto 1988; Jones et al. 2014; Woosley & Heger 2015 and references therein). In this work, we assume that every time a major fuel (C, NeO, Si) is ignited off-center, burning propagates as a convectively bounded flame (CBF). More specifically, once the speed and width of the burning flame are assumed, a given amount of energy in the radiative layers below the convective bound is deposited following the prescription of Woosley & Heger (2015).

We adopt the commonly used mass-loss rate provided by Blöcker (1995; Equation (17) with $\eta = 0.05$) during the AGB and SAGB phases (see, e.g., Jones et al. 2013; Doherty et al. 2015, 2017). This mass-loss rate adds to the other prescriptions already adopted in Limongi & Chieffi (2018).

The initial composition adopted for the solar metallicity is the one provided by Asplund et al. (2009), which corresponds to a total metallicity of $Z = 1.345 \times 10^{-2}$. The adopted initial He mass fraction is 0.265.

3. Results

We computed the evolution of solar metallicity nonrotating stars with initial mass between 7 and 15 $M_\odot$ from the pre-main-sequence phase up to the presupernova stage or an advanced stage during the TP phase, depending on the initial mass. The main evolutionary properties of all of the computed models are reported in Table 2 for stars with initial mass between 7 and 9.20 $M_\odot$ and Table 3 for stars with initial mass between 9.22 and 15 $M_\odot$. The meanings of the various entries (in most cases) are as follows: $M_{\rm CC}$ is the maximum size of the convective core in units of $M_\odot$; t is the evolutionary time in units of years; ^{12}C is the central carbon mass fraction (this entry is reported only for the He-burning phase and refers to the value at core He depletion); $M_{\rm Fe}$, $M_{\rm Si-S}$, $M_{\rm ONe}$, $M_{\rm CO}$, $M_{\rm He}$, $M_{\rm CE}$, and $M_{\rm tot}$ are the iron core mass, Si–S (O-depleted) core mass, ONe core mass, CO core mass, He core mass, convective envelope mass, and total mass, respectively, in units of $M_\odot$; ψ_c, T_c (kelvin), ρ_c (g cm^{-3}), and $Y_{e,c}$ are the central values of the degeneracy parameter, temperature, density, and electron fraction; $T_{\rm ign}$ (kelvin), $\rho_{\rm ign}$ (g cm^{-3}), $\psi_{\rm ign}$, and $M_{\rm ign}$ ($M_\odot$) are the temperature, density, degeneracy parameter, and mass coordinate corresponding to an off-center nuclear ignition; $M_{\rm C}$, reported among the quantities at the end of the second dredge-up in Table 2 and at neon ignition in Table 3, refers to the mass coordinate, in units of $M_\odot$, marking the central zone where the carbon mass fraction exceeds 0.01 (this quantity is relevant for those stars that form hybrid CO/ONeMg cores, i.e., cores mainly composed of ONeMg but with a central region still rich in C).

3.1. Evolution during Core H and He Burning

The evolution of all of the computed models during core H burning is characterized, as usual, by the formation of a convective core that progressively recedes in mass. As a consequence at core H depletion, a He core is formed, surrounded by a zone with a gradient of chemical composition (Figure 1). As H burning shifts progressively in a shell, all of the stars move to the red side of the H-R diagram (Figure 2) and become red giants. During this phase of the evolution, the surface temperature decreases, inducing the formation of a convective envelope that penetrates progressively in mass. When the convective envelope reaches the region of variable composition left by the receding H convective core, a dredge-up to the surface of the products of the core H burning begins (first dredge-up; see Figure 1).

In all of the models, the core He burning starts after the first dredge-up, i.e., when the star is a red giant, and develops in a convective core that, at variance with core H burning, increases progressively in mass (Figure 1). Such an increase, due to the increase of the opacity as a result of the conversion of He into C and O, produces a sharp discontinuity in the radiative gradient at the edge of the convective core that drives the so-called induced overshooting; i.e., the zone homogenized by convection extends beyond the formal border of the convective core, until the neutrality of the radiative and adiabatic gradients is realized (Castellani et al. 1985). During the late stages of core He burning, i.e., when the central He mass fraction decreases below ∼0.1, the fresh He engulfed by the increasing convective core becomes comparable to the central He mass fraction, and this produces a burst of nuclear energy that, in turn, drives a so-called breathing pulse, i.e., a progressive increase of both the convective core and the central He mass fraction. This occurs until the He ingested no longer produces a substantial increase of the nuclear energy (Castellani et al. 1985). Since the occurrence of the breathing pulses is still highly uncertain, they have been suppressed, as already mentioned in Section 2.

During core He burning, models with mass lower than 9.20 $M_\odot$ perform an extended blue loop in the H-R diagram (Figure 2) that is accompanied by a temporary recession and disappearance of the convective envelope when the stars cross the blue side of the H-R diagram (Figure 1). The H shell during core He burning is active and advances in mass, progressively increasing the size of the He core. At core He depletion, all of the models are red giants, and their He core mass is increased by ∼50%, with respect to the one at core H depletion (Figure 3). The CO core at core He depletion increases with the initial mass (see Figure 4, black line, and Tables 2 and 3), ranging between ∼0.5 and ∼2.6 $M_\odot$, while the ^{12}C mass fraction left by the core He burning decreases smoothly with the initial mass and ranges between ∼0.5 and ∼0.38 (see Figure 5, black line, and Tables 2 and 3).

3.2. Evolution after Core He Depletion

The evolution after core He depletion is characterized by the following processes: (1) the shift of the He-burning shell, outward in mass, that progressively increases the size of the CO core and switches off the H-burning shell; (2) the substantial energy loss from the central zones due to the neutrino emission; (3) the energy deposition in the more

Table 2
Main Properties of the Computed Models

	7.00	7.50	8.00	8.50	8.80	9.00	9.05	9.10	9.15	9.20
					H Burning					
M_{CC}	2.38	2.55	2.78	3.01	3.12	3.25	3.27	3.29	3.30	3.32
t	5.04(7)	4.35(7)	3.83(7)	3.4(7)	3.18(7)	3.05(7)	3.02(7)	2.98(7)	2.95(7)	2.93(7)
M_{He}	1.13	1.21	1.31	1.45	1.54	1.63	1.63	1.64	1.65	1.66
M_{tot}	6.97	7.47	7.96	8.46	8.76	8.96	9.01	9.06	9.11	9.16
					He Ignition					
M_{He}	1.15	1.28	1.41	1.55	1.61	1.67	1.68	1.69	1.71	1.73
M_{CE}	1.74	1.91	2.10	2.26	2.37	2.47	2.49	2.52	2.55	2.57
					He Burning					
M_{CC}	0.70	0.76	0.84	0.92	0.98	1.03	1.05	1.06	1.07	1.09
t	4.85(6)	4.12(6)	3.45(6)	2.98(6)	2.76(6)	2.62(6)	2.61(6)	2.58(6)	2.54(6)	2.51(6)
^{12}C	0.487	0.481	0.471	0.463	0.458	0.456	0.454	0.453	0.453	0.454
M_{CO}	0.69	0.76	0.84	0.92	0.98	1.02	1.04	1.06	1.07	1.08
M_{He}	1.76	1.91	2.09	2.26	2.36	2.44	2.47	2.48	2.49	2.46
M_{CE}	3.43	3.67	3.94	4.13	4.21	4.35	4.39	4.24	4.12	3.44
M_{tot}	6.82	7.30	7.77	8.25	8.54	8.71	8.75	8.79	8.83	8.86
					Quantities at Carbon Ignition					
$\mathrm{Log}(T_{ign})$		8.827	8.823	8.836	8.843	8.839	8.832	8.839	8.823	8.842
$\mathrm{Log}(\rho_{ign})$		6.142	6.133	6.136	6.131	6.132	6.132	6.131	6.136	6.129
ψ_{ign}		2.527	2.520	2.451	2.348	2.465	2.443	2.376	2.533	2.348
M_{ign}		0.588	0.431	0.289	0.204	0.157	0.134	0.115	0.107	0.088
M_{CO}		1.056	1.114	1.182	1.226	1.258	1.269	1.276	1.287	1.294
M_{He}		1.083	1.216	2.200	2.326	2.372	2.391	2.432	2.455	2.438
M_{CE}		1.083	1.216	2.259	2.380	2.461	2.481	2.500	2.521	2.520
M_{tot}		7.241	7.718	8.197	8.480	8.650	8.732	8.731	8.769	8.794
					Quantities at the End of Second Dredge-up					
^{12}C		0.481	0.470	0.462	0.455	0.016	0.014	0.014	0.005	0.004
M_C		0.232	0.065	0.033	0.013	0.000	0.000	0.000	0.000	0.000
M_{ONe}		1.03316	1.11495	1.21184	1.27128	1.31519	1.32877	1.33812	1.34922	1.35563
M_{CO}	1.01410	1.07167	1.15622	1.22877	1.28056	1.31805	1.33208	1.34116	1.35171	1.35798
M_{He}	1.02303	1.07514	1.15917	1.22877	1.28056	1.31805	1.33208	1.34116	1.35171	1.35798
M_{CE}	1.02304	1.07515	1.15918	1.22877	1.28056	1.31805	1.33208	1.34116	1.35171	1.35798
M_{tot}	6.725	7.206	7.678	8.159	8.441	8.592	8.616	8.677	8.712	8.736
$\mathrm{Log}(\rho_c)$	7.107	7.423	7.722	8.076	8.359	8.738	8.794	8.843	8.940	8.976
$\mathrm{Log}(\rho\ Y_e)_c$	6.806	7.121	7.421	7.775	8.058	8.435	8.491	8.541	8.637	8.673
$\mathrm{Log}(T_c)$	8.354	8.305	8.378	8.462	8.539	8.554	8.601	8.632	8.663	8.692
					Quantities at First Thermal Pulse					
M_{ONe}		1.03316	1.13398	1.21795	1.27580	1.31578	1.33056	1.33995	1.35082	1.35727
M_{CO}	1.02490	1.07682	1.16041	1.22968	1.28106	1.31835	1.33234	1.34138	1.35192	1.35813
M_{He}	1.02592	1.07735	1.16062	1.22977	1.28111	1.31837	1.33235	1.34140	1.35193	1.35813
M_{CE}	1.02609	1.07740	1.16063	1.22977	1.28111	1.31837	1.33235	1.34140	1.35193	1.35813
M_{tot}	6.654	7.154	7.635	8.109	8.380	8.541	8.588	8.627	8.665	8.692
$\mathrm{Log}(\rho_c)$	7.405	7.631	7.969	8.290	8.590	8.879	9.016	9.118	9.236	9.331
$\mathrm{Log}(\rho\ Y_e)_c$	7.103	7.330	7.667	7.989	8.288	8.576	8.713	8.815	8.932	9.026
$\mathrm{Log}(T_c)$	8.222	8.240	8.284	8.347	8.413	8.466	8.509	8.172	8.767	8.406
$^4He_{sup}$	0.378	0.384	0.374	0.391	0.394	0.395	0.395	0.395	0.395	0.394
$^{12}C_{sup}$	1.18(−3)	1.18(−3)	1.19(−3)	2.02(−3)	2.02(−3)	2.34(−3)	3.95(−3)	2.66(−3)	2.78(−3)	2.86(−3)
$^{14}N_{sup}$	3.18(−3)	3.23(−3)	3.23(−3)	3.32(−3)	3.35(−3)	3.32(−3)	2.51(−3)	3.25(−3)	3.25(−3)	3.21(−3)
$^{16}O_{sup}$	4.43(−3)	4.38(−3)	4.37(−3)	4.67(−3)	4.56(−3)	4.56(−3)	4.54(−3)	4.59(−3)	4.59(−3)	4.61(−3)

Note. In the H- and He-burning sections, all of the quantities refer to the values at the end of each nuclear burning, the only exception being M_{CC}, which is the maximum extension in mass of the convective core during the nuclear burning, and t, which is the evolutionary time of each burning stage.

external zones of the CO core due to compressional heating induced by the advancing of the He-burning shell; and (4) the progressive penetration of the convective envelope that may eventually produce the second dredge-up. The interplay and timing of these processes and the final fate of the star depend on the CO core mass at core He depletion that, in turn,

Table 3
Main Properties of the Computed Models

	9.22	9.25	9.30	9.50	9.80	10.00	11.00	12.00	13.00	15.00
					H Burning					
M_{CC}	3.33	3.34	3.36	3.57	3.68	3.76	4.18	4.75	5.28	6.45
t	2.91(7)	2.90(7)	2.87(7)	2.76(7)	2.60(7)	2.51(7)	2.11(7)	1.83(7)	1.62(7)	1.31(7)
M_{He}	1.66	1.66	1.72	1.76	1.84	1.88	2.19	2.56	2.91	3.71
M_{tot}	9.18	9.21	9.26	9.46	9.76	9.96	10.90	11.90	12.90	14.88
					He Ignition					
M_{He}	1.73	1.74	1.77	1.81	1.89	1.94	2.24	2.57	2.91	3.66
M_{CE}	2.75	2.59	2.61	2.69	2.78	2.84	3.24	3.67	4.13	5.12
					He Burning					
M_{CC}	1.09	1.10	1.11	1.16	1.21	1.25	1.49	1.82	2.11	2.71
t	2.50(6)	2.48(6)	2.46(6)	2.36(6)	2.21(6)	2.12(6)	1.74(6)	1.51(6)	1.30(6)	1.01(6)
^{12}C	0.454	0.452	0.451	0.446	0.446	0.444	0.434	0.413	0.404	0.388
M_{CO}	1.08	1.10	1.11	1.16	1.20	1.24	1.48	1.82	2.10	2.71
M_{He}	2.47	2.48	2.50	2.57	2.66	2.73	3.10	3.51	3.91	4.80
M_{CE}	3.43	3.41	3.40	3.39	3.54	3.63	3.84	4.21	4.55	5.45
M_{tot}	8.88	8.90	8.95	9.13	9.42	9.61	10.39	11.26	12.13	13.91
					Quantities at Carbon Ignition					
$\mathrm{Log}(T_{ign})$	8.841	8.838	8.847	8.832	8.833	8.827	8.833	8.835	8.826	8.855
$\mathrm{Log}(\rho_{ign})$	6.129	6.133	6.122	6.135	6.133	6.093	5.887	5.687	5.552	5.383
ψ_{ign}	2.354	2.395	2.270	2.453	2.438	2.313	1.440	0.741	0.369	-0.250
M_{ign}	0.085	0.075	0.060	0.022	0.000	0.000	0.000	0.000	0.000	0.000
M_{CO}	1.297	1.302	1.313	1.355	1.379	1.398	1.598	1.877	2.127	2.708
M_{He}	2.443	2.455	2.475	2.550	2.635	2.695	3.083	3.486	3.895	4.779
M_{CE}	2.527	2.543	2.563	2.644	2.732	2.805	3.223	3.640	4.071	5.020
M_{tot}	8.814	8.838	8.882	9.060	9.345	9.531	10.356	11.160	11.981	13.647
					Quantities at Neon Ignition					
^{12}C	0.004	0.004	0.003	0.002	0.000	0.000	0.000	0.000	0.000	0.000
M_C	0.000	0.000	0.000	0.000	0.000	0.000	0.000	0.000	0.000	0.000
$\mathrm{Log}(T_{ign})$	9.144	9.152	9.147	9.154	9.150	9.158	9.152	9.156	9.152	9.147
$\mathrm{Log}(\rho_{ign})$	7.462	7.440	7.428	7.410	7.351	7.333	7.263	7.219	7.173	6.971
ψ_{ign}	6.714	6.417	6.419	6.171	5.810	5.579	5.192	4.874	4.640	3.586
M_{ign}	0.966	0.921	0.872	0.642	0.545	0.538	0.176	0.026	0.000	0.000
M_{ONe}	1.34946	1.35567	1.36681	1.39495	1.41473	1.45264	1.61811	1.78829	2.00073	2.38106
M_{CO}	1.36292	1.36870	1.38197	1.42102	1.45570	1.48738	1.71252	1.93653	2.29977	2.38106
M_{He}	1.51131	1.52312	1.54993	1.72901	1.86507	2.42851	3.05750	3.45724	3.88738	4.77346
M_{CE}	1.51200	1.52370	1.55042	1.72952	1.86562	2.42956	3.18014	3.60951	4.01319	4.99950
M_{tot}	8.741	8.780	8.821	8.960	9.257	9.433	10.238	11.041	11.877	13.575
					Quantities at Si–S Ignition					
$\mathrm{Log}(T_{ign})$	9.525	9.489	9.474	9.498	9.506	9.529	9.540	9.490	9.530	9.527
$\mathrm{Log}(\rho_{ign})$	8.191	8.789	9.032	9.171	8.711	9.004	8.474	8.462	8.455	8.390
ψ_{ign}	5.50	10.78	13.90	16.17	9.622	11.88	7.069	7.935	7.152	6.724
M_{ign}	0.950	0.518	0.074	0.005	0.387	0.034	0.329	0.156	0.000	0.000
M_{Si-S}	1.28952	1.32611	1.15688	1.30951	1.26548	1.29341	1.30356	1.35927	1.34362	1.41895
M_{ONe}	1.34885	1.36052	1.36940	1.40788	1.44591	1.47493	1.65900	1.91495	2.13818	2.58421
M_{CO}	1.36285	1.36866	1.37739	1.42064	1.45538	1.48721	1.69211	1.97370	2.22577	2.78635
M_{He}	1.50705	1.52163	1.54957	1.72741	1.86312	2.42734	3.10849	3.50850	3.91748	4.80126
M_{CE}	1.50779	1.52218	1.54989	1.72799	1.86375	2.46322	3.18014	3.60951	3.99913	4.99799
M_{tot}	8.741	8.780	8.821	8.960	9.256	9.433	10.237	11.041	11.877	13.575
$\mathrm{Log}T_c$	9.165	8.971	9.046	9.482	9.386	9.314	9.418	9.459	9.530	9.527
$\mathrm{Log}\rho_c$	9.358	9.367	9.158	9.291	9.146	9.072	8.855	8.666	8.455	8.390
$\mathrm{Log}(\rho Y_e)_c$	9.035	9.035	8.830	8.959	8.815	8.750	8.525	8.338	8.134	8.067
					Quantities at Presupernova Stage					
M_{Fe}	1.258	1.262	1.263	1.268	1.275	1.276	1.295	1.313	1.372	1.388
$\mathrm{Log}(T_c)$	9.837	9.833	9.825	9.838	9.833	9.839	9.834	9.834	9.817	9.821

Table 3
(Continued)

	9.22	9.25	9.30	9.50	9.80	10.00	11.00	12.00	13.00	15.00
$\mathrm{Log}(\rho_c)$	9.742	9.742	9.819	9.719	9.685	9.654	9.602	9.550	9.551	9.441
ψ_c	10.63	10.72	11.68	10.40	10.22	9.79	9.48	9.04	9.44	8.47
$Y_{e,c}$	0.422	0.441	0.440	0.441	0.440	0.440	0.440	0.441	0.440	0.441

Note. Same as in Table 2.

depends on the He core mass at core H depletion and, ultimately, on the initial mass.

3.3. Evolution toward the TP-AGB Phase: Stars with Initial Mass $\mathrm{M} \leqslant 7.0\,\mathrm{M}_\odot$ ($\mathrm{M}_{CO} \leqslant 0.69\,\mathrm{M}_\odot$)

In stars with initial mass $M \leqslant 7.0\,M_\odot$ (that form CO cores at core He exhaustion with $M_{\mathrm{CO}} \leqslant 0.69\,M_\odot$), the maximum temperature within the CO core does not reach the threshold value for C ignition, the CO core becomes progressively more and more degenerate, and eventually, these stars enter the TP-AGB phase. We followed the evolution of the $7\,M_\odot$ model along 27 thermal pulses. The evolution of solar metallicity AGB stars with mass around $7\,M_\odot$ has already been discussed in detail in the literature (see Section 1); therefore, we will not address them here, but we report in Table 2 the main properties of the model at various key times during the evolution. Figures 2 and 6 show the evolutionary path of the model in the H-R diagram and the central temperature–central density plane. It is worth mentioning the occurrence of the second dredge-up starting after core He depletion and going to completion before the onset of the TPs. The effect of the second dredge-up is that of reducing the He core from $1.76\,M_\odot$ (value at core He depletion) to $1.01\,M_\odot$ (Figure 3).

The main properties of the thermal pulse phase are reported in Table 4 and the upper left panels of Figures 7–10. The values reported in the table, as well as the behavior of the various quantities shown in the figures, are consistent with what has been found in the literature (see Section 1). Let us note only that the maximum temperature at the base of the convective envelope increases progressively from ∼40 MK at the beginning of the TP phase to a plateau value corresponding to ∼80 MK after the first ∼16 TPs (upper left panel of Figure 9). By the way, Nomoto & Sugimoto (1972) investigated in their Figures 2 and 3 how the temperature at the base of the convective envelope and the depth of mixing depends on the luminosity and mass of the CO core. The third dredge-up, due to the penetration of the convective envelope into the He core during the quiescent shell He-burning phase, i.e., when the H-burning shell is switched off, occurs after a few TPs and induces from one side a progressive reduction of the rate at which the CO core increases (upper left panel of Figure 8) and, at the same time, a progressive enrichment of the surface carbon abundance (upper left panel of Figure 10). Note, however, that such an enhancement is very mild; in fact, the surface carbon abundance has increased at the end of this phase by a factor of ∼1.1 compared to the value at core He depletion. For this reason, we decided to not take into account carbon-enhanced opacity tables. By the way, let us remember that, as already mentioned in Section 2, we assume some amount of extra mixing at the base of the convective envelope; therefore, this is also applied during the third dredge-up. Figure 11 shows the behavior of the convective zones during the last thermal pulses before the end of the calculation, where one can appreciate the size of the He convective shell that forms after the He shell ignition and the efficiency of the third dredge-up, in particular the quantity $\lambda = \Delta M_{\mathrm{dredge}}/\Delta M_{\mathrm{H}} \sim 0.78$, where ΔM_{H} is the increase of the core mass during the interpulse phase and $\Delta M_{\mathrm{dredge}}$ is the maximum penetration of the convective envelope following the pulse (see, e.g., Figure 5 in Doherty et al. 2017).

3.4. Evolution during C Burning: Stars with Initial Mass $\mathrm{M} \geqslant 7.5\,\mathrm{M}_\odot$ ($\mathrm{M}_{CO} \geqslant 0.76\,\mathrm{M}_\odot$)

In stars with initial mass $M \geqslant 7.5\,M_\odot$ (CO core masses at core He depletion $M_{\mathrm{CO}} \geqslant 0.76\,M_\odot$), the maximum temperature within the CO core reaches the threshold value for the C-burning ignition. Depending on the initial mass, C ignition may occur in the center or off-center in a (partial) degenerate environment.

In stars with initial mass $7.5 \leqslant M/M_\odot \leqslant 9.5$ ($0.76 \leqslant M_{\mathrm{CO}}/M_\odot \leqslant 1.16$), the interplay between processes 2 and 3 (see above) induces the formation of an off-center peak temperature that progressively increases locally and moves outward in mass while the CO core becomes progressively more degenerate. Therefore, for these stars, the C ignition occurs off-center, and, in general, as the initial mass increases, the mass coordinate corresponding to the ignition point becomes closer to the center, ranging from 0.59 to $0.02\,M_\odot$ for the 7.5 and $9.5\,M_\odot$ models, respectively (black line in Figure 12). The off-center ignition is generally accompanied by the formation of a convective zone driven by the high flux produced by the C-burning reactions in a (partial) degenerate environment ($\psi_{\mathrm{ign}} \sim 2.5$; see Table 2). When the energy flux produced by the nuclear burning reduces, the convective zone vanishes. The disappearance of this convective shell is then followed by a number of other convective zones associated with the C-burning front that progressively moves toward the center and locally removes the degeneracy. In general, the number of convective zones that follow the first one decreases as the initial mass of the star increases (Figure 1). Typical internal structures corresponding to two different stages during this phase are shown in Figures 13 and 14 for the $8.5\,M_\odot$ model. Note that ^{12}C is not completely exhausted in the zones where the C-burning front has passed. The C-burning front, marked by the maximum temperature, reaches the center in stars with initial mass $M \geqslant 9.2\,M_\odot$ and then begins moving outward in mass where ^{12}C is still abundant, again inducing the formation of a number of successive convective shells (Figure 1). In the lower-mass models, on the contrary, the maximum temperature never reaches the center. However, the following shell C-burning phase develops in these stars similarly to the more massive ones. In all of these models, after the last C convective episode, C burning proceeds in a radiative shell, progressively reducing the CO-rich zone

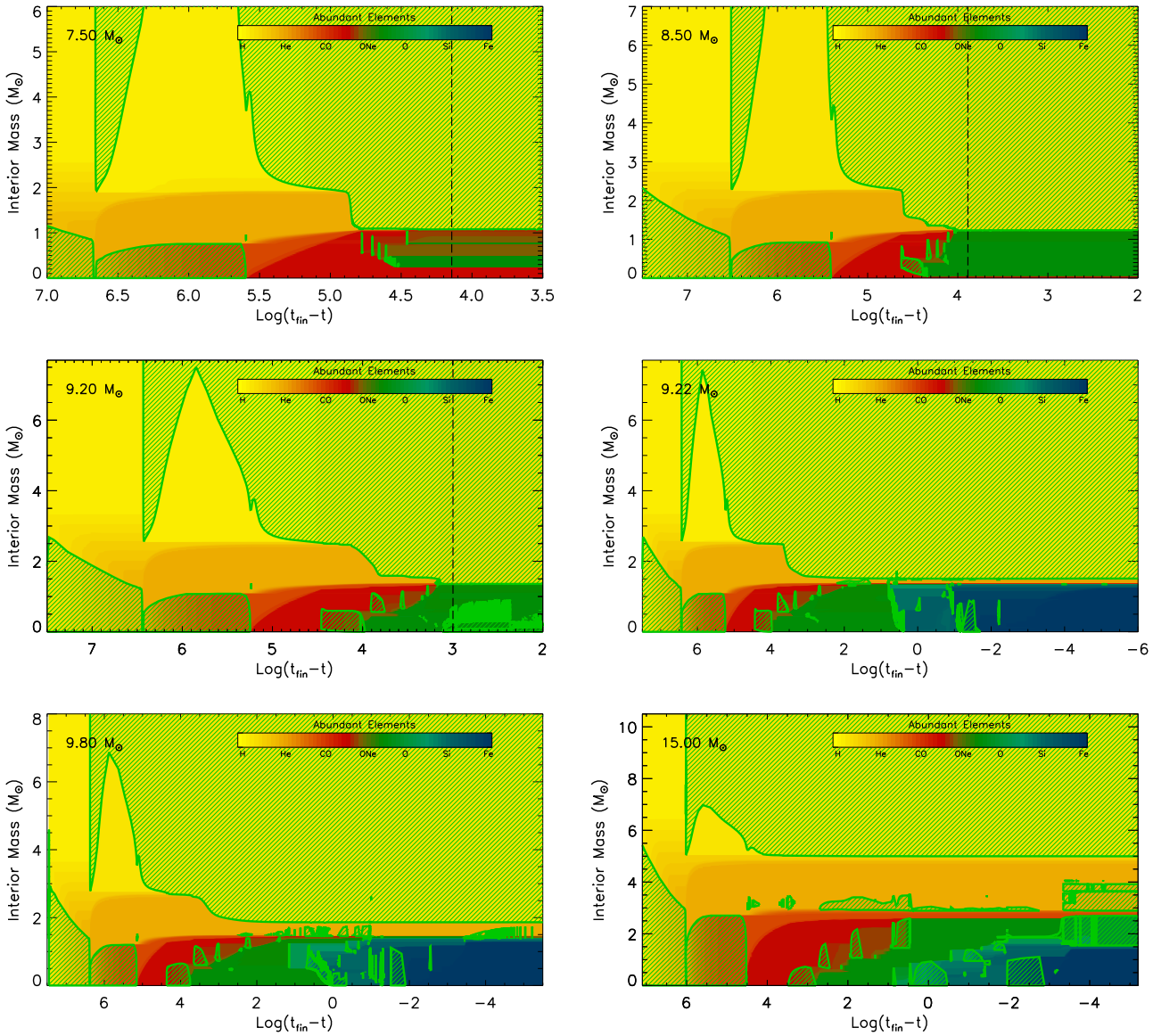

Figure 1. Convective (green shaded areas) and chemical (color codes reported in the color bar) internal history of selected models from the main-sequence phase up to an advanced stage of the TP-SAGB phase (top and middle left panels) or the onset of the iron core collapse prior to the CCSN explosion (middle right and bottom panels). The dashed line in the top and middle left panels marks the onset of the TP phase. The *x*-axis reports the logarithm of the time until the end of the evolution ($t_{\rm fin} - t$) in units of years.

confined between the ONeMg core resulting from the shell C burning and the He-rich zone (the red zone in Figure 15). It is worth noting that in all of these models, some ^{12}C remains unburned in the central zone. The mass fraction of the unburned ^{12}C, as well as the mass of the core where this quantity is larger than 0.01, decreases with increasing initial mass. In particular, Figure 5 (blue line) shows that the mass of the central zone where the ^{12}C mass fraction is larger than 0.01 decreases from $\sim$0.33 $M_\odot$ in the 7.5 $M_\odot$ model to $\sim$0.01 $M_\odot$ in the 8.8 $M_\odot$ model and disappears for larger initial masses. Figure 1 shows how the configuration of the ONeMg (green shaded areas)/CO (red shaded areas) cores changes as a function of the initial mass.

In stars with initial mass $M \geqslant 9.8\,M_\odot$ (CO core masses at core He depletion $M_{\rm CO} \geqslant 1.2\,M_\odot$), C burning is ignited in the center and develops in a convective core. Once the ^{12}C is depleted in the center, C burning shifts in shell and, as in the case of the lower-mass models, induces the formation of a number of convective shells (Figure 1). These stars behave like the classical MSs (Limongi & Chieffi 2018; Chieffi & Limongi 2020).

3.5. Evolution of the Convective Envelope: Stars with Initial Mass $\mathrm{M} \leqslant 10.0\,\mathrm{M}_\odot$ ($\mathrm{M}_{CO} \leqslant 1.20\,\mathrm{M}_\odot$)

As already mentioned in Section 3.2, after core He depletion, the H-burning shell is switched off by the advancing He-burning shell, and this may induce the convective envelope to penetrate into the He-rich layer (second dredge-up). This phenomenon occurs only in stars with initial mass $M \leqslant 10\,M_\odot$, although in different evolutionary stages (see also Section 4.2 and Figure 4.3 of Sugimoto & Nomoto 1980, for a discussion on the mechanism of the convective penetration). More specifically, the second dredge-up begins (1) before carbon ignition and goes to completion after carbon burning in stars

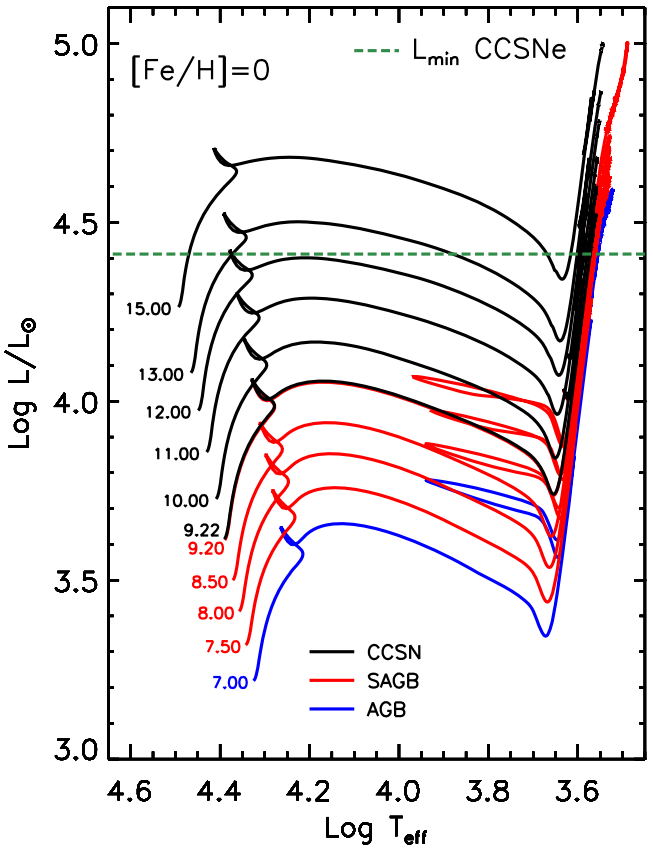

Figure 2. Evolutionary path in the H-R diagram of selected models. The blue line refers to the AGB star, i.e., the one that develops a degenerate CO core, does not ignite C burning, and enters the TP phase. The red lines refer to SAGB stars, i.e., those that ignite C burning and then do not ignite Ne burning; these stars develop a degenerate ONeMg core and enter the TP phase. The black lines refer to those stars that ignite Ne burning and eventually explode as CCSNe. The horizontal green dashed line marks the final luminosity of the lowest mass that explodes as CCSNe, i.e., the expected minimum luminosity of CCSNe (Smartt 2015).

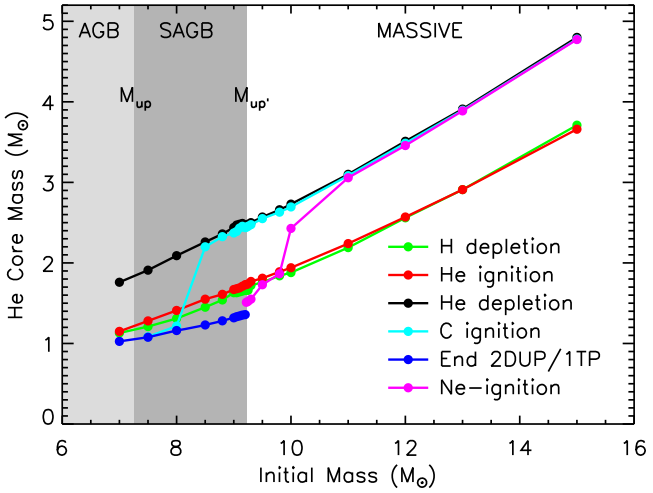

Figure 3. He core mass at various evolutionary stages (see legend).

with initial mass $7.5 \leqslant M/M_{\odot} \leqslant 8.0$ (compare the black line with the cyan and blue lines in Figure 3) and (2) after carbon ignition and goes to completion after carbon burning in stars with initial mass $8.5 \leqslant M/M_{\odot} \leqslant 10.0$ (compare the black line

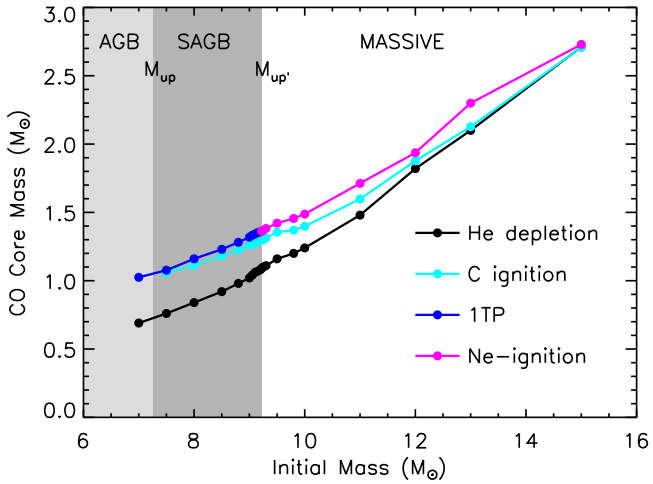

Figure 4. CO core mass at various evolutionary stages (see legend).

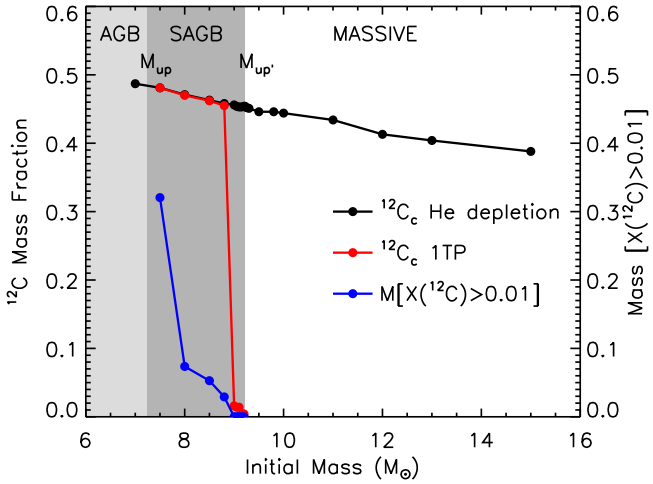

Figure 5. Central ^{12}C mass fraction at core He depletion (black line and dots) and at first thermal pulse (red line and dots). The blue line refers to the mass of the central zone where the ^{12}C mass fraction is larger than 0.01. The figure shows that the models with initial mass between 7.5 and 8.8 $M_{\odot}$ form a hybrid degenerate CO core.

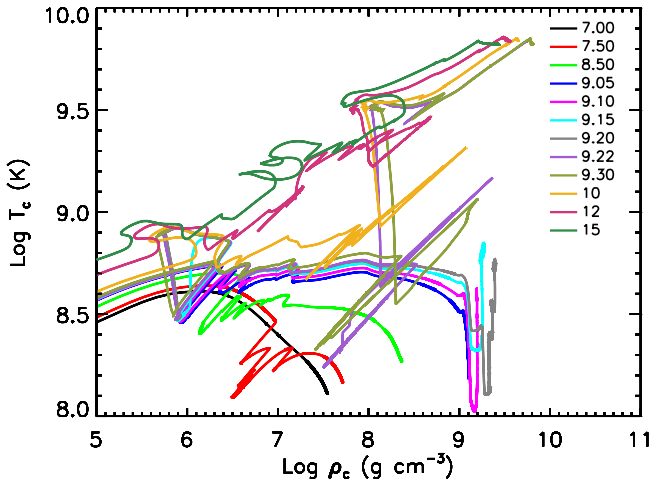

Figure 6. Evolution of the central temperature and density of all of the computed models.

with cyan, blue, and magenta lines in Figure 3). The second dredge-up for stars with initial mass $M \leqslant 7.0\,M_{\odot}$ has already been discussed in Section 3.3 and will not be repeated here.

Table 4
Main Properties of the TP Phase of the 7.00 $M_\odot$ Model

TP	$\Delta t_{\rm pulse}$ (yr)	$\log(L_{\rm He}/L_\odot)^{\rm max}$	$\Delta M_{\rm pulse}^{\rm max}$ ($M_\odot$)	$T_{\rm He}^{\rm max}$ (10^8 K)	λ	$\Delta t_{\rm inter}$ (yr)	$\Delta M_{\rm He}$ ($M_\odot$)	$\Delta M_{\rm CO}$ ($M_\odot$)
1	89.82555	4.59285	0.0000e+00	2.24571	0.00000	0.00000	0.0000e+00	0.0000e+00
2	111.22892	4.96992	6.3260e–04	2.28490	0.00000	810.01669	3.3420e–04	3.4780e–04
3	115.42192	5.16239	7.6520e–04	2.39542	0.00000	830.90516	3.5400e–04	3.7560e–04
4	117.34890	5.32072	8.2270e–04	2.46989	0.00000	864.45584	3.7510e–04	3.9770e–04
5	121.55523	5.45162	8.3630e–04	2.51289	0.00000	893.41053	3.9600e–04	4.1390e–04
6	111.21537	5.56693	8.6150e–04	2.55107	0.07813	913.12543	4.1340e–04	4.2040e–04
7	101.03505	5.67624	8.7040e–04	2.60405	0.16083	940.51568	4.3400e–04	4.0980e–04
8	88.24332	5.77267	2.5130e–04	2.62902	0.23434	970.62890	4.5490e–04	4.4900e–04
9	81.30580	5.87702	5.8090e–04	2.67875	0.30707	1006.22846	4.7840e–04	3.5950e–04
10	74.49517	5.97425	2.3260e–04	2.75055	0.36661	1030.11027	4.9780e–04	3.4330e–04
11	64.23646	6.07593	4.4130e–04	2.78056	0.43756	1055.91787	5.1650e–04	3.2550e–04
12	57.77569	6.17135	4.9130e–04	2.80497	0.48888	1078.39620	5.3510e–04	3.0690e–04
13	51.39315	6.26646	2.6260e–04	2.85028	0.54340	1104.62488	5.5300e–04	2.8640e–04
14	50.50076	6.35809	5.7070e–04	2.89319	0.56731	1128.54045	5.7200e–04	2.6670e–04
15	27.97671	6.44017	0.0000e+00	2.92910	0.61947	1153.48452	5.8760e–04	2.6170e–04
16	26.69483	6.53373	3.4460e–04	2.92627	0.65240	1204.24569	6.0760e–04	2.3630e–04
17	24.99774	6.63534	0.0000e+00	2.96001	0.67273	1256.05894	6.2150e–04	2.1540e–04
18	24.10871	6.73287	1.7150e–04	3.04020	0.70374	1307.67283	6.2850e–04	2.0410e–04
19	22.83511	6.80368	2.4150e–04	3.04617	0.71882	1318.63689	6.4300e–04	1.9780e–04
20	22.59946	6.93882	3.1260e–04	3.05739	0.75870	1528.42922	6.6350e–04	1.9310e–04
21	21.40192	6.93939	3.2010e–04	3.11509	0.72959	1339.37664	6.7230e–04	1.7350e–04
22	21.20829	7.05233	2.9090e–04	3.15358	0.77054	1482.17119	6.8640e–04	1.8030e–04
23	20.61109	7.07359	2.8640e–04	3.17158	0.75515	1404.52193	6.9880e–04	1.7120e–04
24	20.33897	7.17656	2.6540e–04	3.18900	0.78070	1558.92042	7.1590e–04	1.7980e–04
25	20.14531	7.19896	2.5370e–04	3.21168	0.77932	1465.13032	7.2050e–04	1.5830e–04
26	19.13683	7.27968	2.4650e–04	3.22242	0.78318	1587.41454	7.4210e–04	1.7660e–04
27	19.27082	7.32997	2.2530e–04	3.23992	0.80253	1584.22310	7.4340e–04	1.5770e–04

Note. The columns are as follows. TP is the pulse number; $\Delta t_{\rm pulse}$ is the duration of the pulse in years; $\log(L_{\rm He}/L_\odot)^{\rm max}$ is the maximum luminosity provided by the He-burning reactions during the pulse in solar luminosity; $\Delta M_{\rm pulse}^{\rm max}$ is the maximum extension of the He convective shell during the pulse in solar masses; $T_{\rm He}^{\rm max}$ is the maximum temperature of the He-burning shell during the pulse in kelvin; λ is the measure of the efficiency of the third dredge-up and is defined in Section 3.3; $\Delta t_{\rm inter}$ is the time elapsed between two consecutive thermal pulses in years; and $\Delta M_{\rm He}$ and $\Delta M_{\rm CO}$ are the increase of the He and CO core, respectively, in solar masses between two consecutive thermal pulses. The full machine-readable table containing the properties of the 7.00, 7.50, 8.00, 8.50, 8.80, 9.00, 9.05, 9.10, 9.15, and 9.20 $M_\odot$ models is available online.

(This table is available in its entirety in machine-readable form.)

In general, during the second dredge-up, the convective envelope penetrates into the He core and therefore brings to the surface material that has been processed by H burning through the CNO cycle. This means that during this phase, the surface ^{12}C mass fraction decreases, while the surface ^{14}N mass fraction increases (Figure 10).

In stars with initial mass $8.50 \leqslant M/M_\odot \leqslant 9.20$, the C-burning shell is efficient enough to progressively switch off the He-burning shell. As a consequence, in these stars, the convective envelope penetrates deep enough to dredge up the products of the He burning. Once this deep penetration occurs, the surface abundance of ^{12}C suddenly increases, while that of ^{14}N progressively decreases (see Figure 10). In general, the larger the mass, the larger the increase of the surface ^{12}C abundance.

It is worth noting that in stars with $8.8 \leqslant M/M_\odot \leqslant 9.20$ ($0.98 \leqslant M_{\rm CO}/M_\odot \leqslant 1.08$), a He convective shell forms during the second dredge-up. Such an occurrence slightly slows down the penetration of the convective envelope into the He core. Once the He convective shell disappears, the penetration resumes (Figure 15), and the products of the He burning, mainly (primary) ^{12}C (Figure 10), are mixed up to the surface. Note that, in this case, the increase of the surface ^{12}C abundance at the end of the second dredge-up is mainly due to the penetration of the convective envelope into the extinguished He convective shell and, to a lesser extent, the penetration into the CO core. The dredge-up of the He-burning products has been named "corrosive second dredge-up" by Gil-Pons et al. (2013) and Doherty et al. (2014), but we instead refer to it as an early third dredge-up (E3DU) because this phenomenon is identical to the one occurring during the interpulse phase of TP-AGB stars (see above), although in this case it occurs well before the beginning of the onset of the thermal pulses (see below). It is worth noting that in none of these models do the He convective shell and the convective envelope interact with each other; i.e., we do not find the so-called "dredge-out" episode, a phenomenon found for the first time by Ritossa et al. (1999) and later in other studies (see, e.g., Siess 2007; Gil-Pons et al. 2013; Doherty et al. 2015; Jones et al. 2016). This is probably due to the fact that while in the previously mentioned studies, a convective overshooting is considered for any convective zone (cores and shells), in these calculations, we assume some amount of extra mixing only at the edge of the H convective core, at the base of the convective envelope, and at the base of the convective shells during any off-center ignition (see Section 2). As a final comment, we point out that in all of the models mentioned above, the increase of the surface carbon abundance due to the E3DU is in any case very mild. In the 9.2 $M_\odot$ model, where the E3DU produces the largest effects, the enhancement of the surface

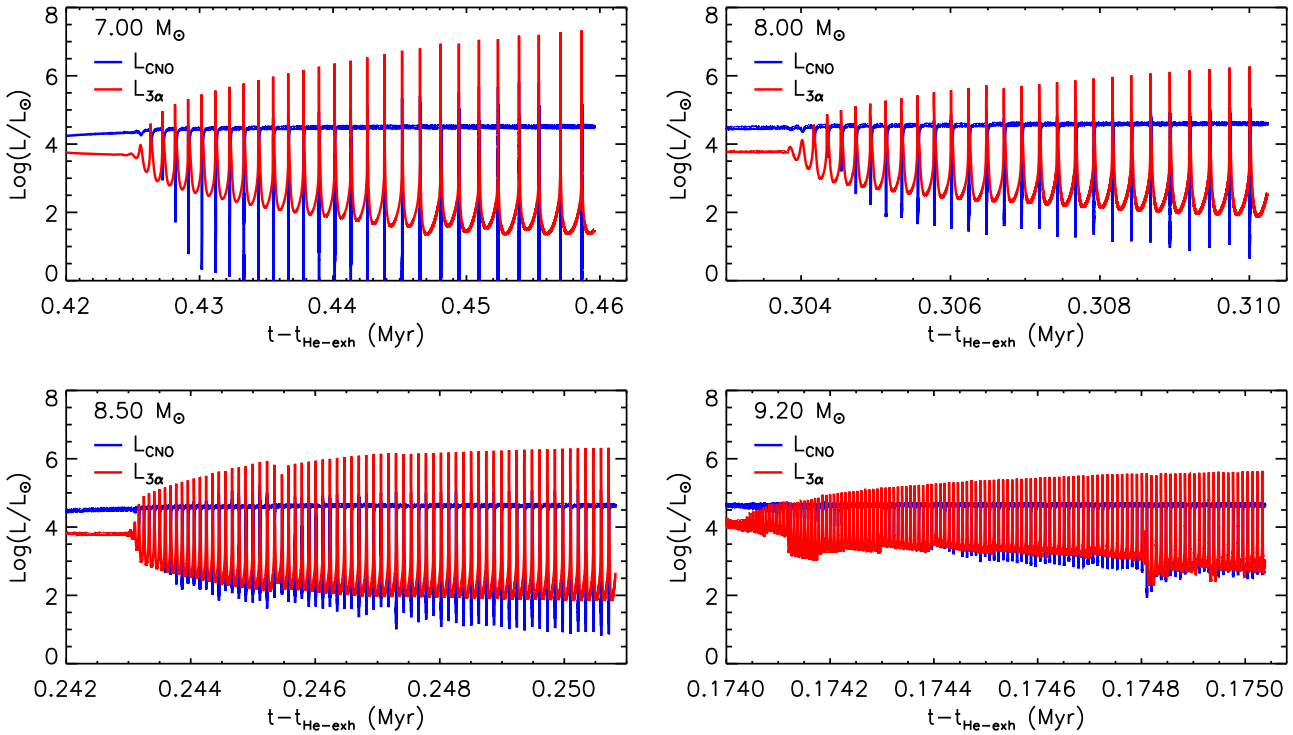

Figure 7. Evolution of the H (blue line) and He (red line) luminosities as a function of time during the AGB phase (for the 7.0 $M_{\odot}$ model; upper left panel) and the SAGB phase (for the 8.0, 8.5, and 9.2 $M_{\odot}$ models; upper right, lower left, and lower right panels, respectively). The time has been reset at the core He exhaustion.

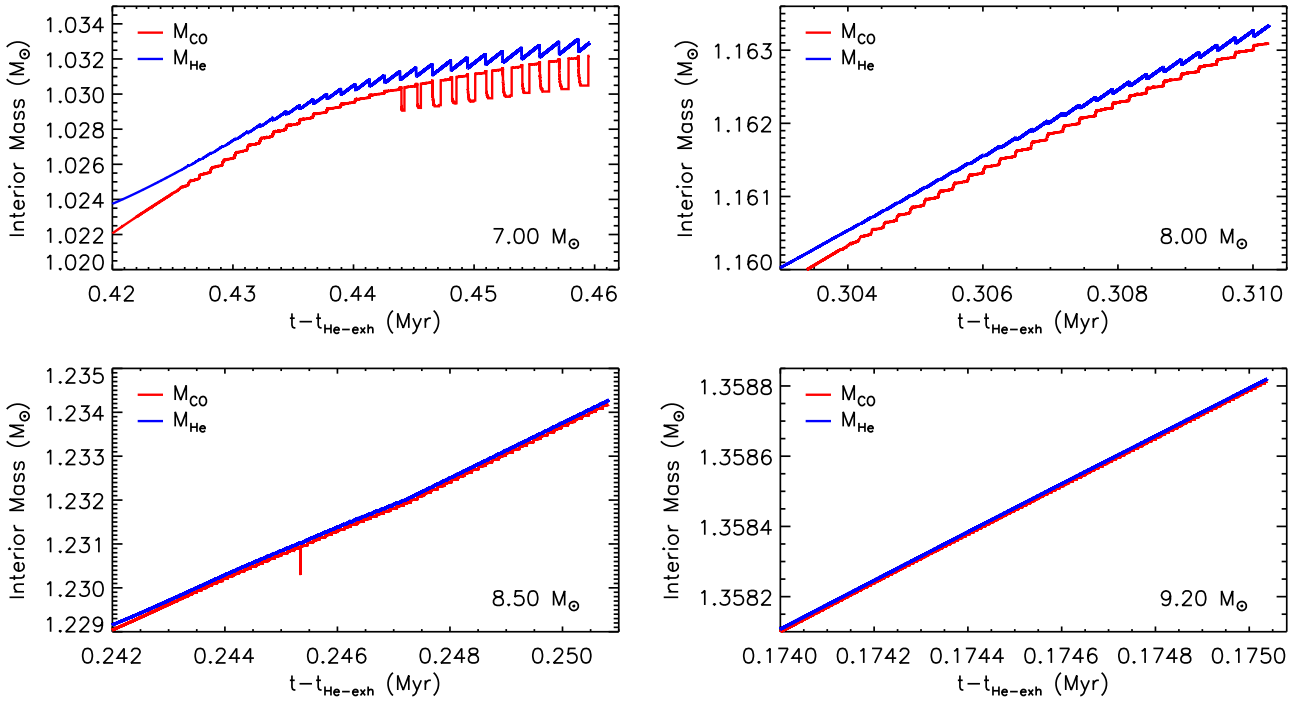

Figure 8. Evolution of the He (blue line) and C (red line) core masses as a function of time during the AGB phase (for the 7.0 $M_{\odot}$ model; upper left panel) and the SAGB phase (for the 8.0, 8.5, and 9.2 $M_{\odot}$ models; upper right, lower left, and lower right panels, respectively). The time has been reset at the core He exhaustion.

carbon abundance is a factor of ∼2 compared to the value at core He depletion. Since during the first dredge-up, the surface carbon abundance decreases by a factor of ∼2 compared to the initial one, the result is that the surface carbon mass fraction after the E3DU is roughly equal to the initial one. For this reason, also in this case, we decided to not take into account carbon-enhanced opacity tables.

In all of the stars with initial mass $7.5 \leqslant M/M_{\odot} \leqslant 9.2$, during the second dredge-up, the envelope expands and cools down in order to reabsorb the energy produced by the more internal nuclear burning shells. However, the rate at which the convective envelope penetrates in mass is higher than the rate at which it cools down; therefore, the temperature at the base of the convective envelope increases progressively until the

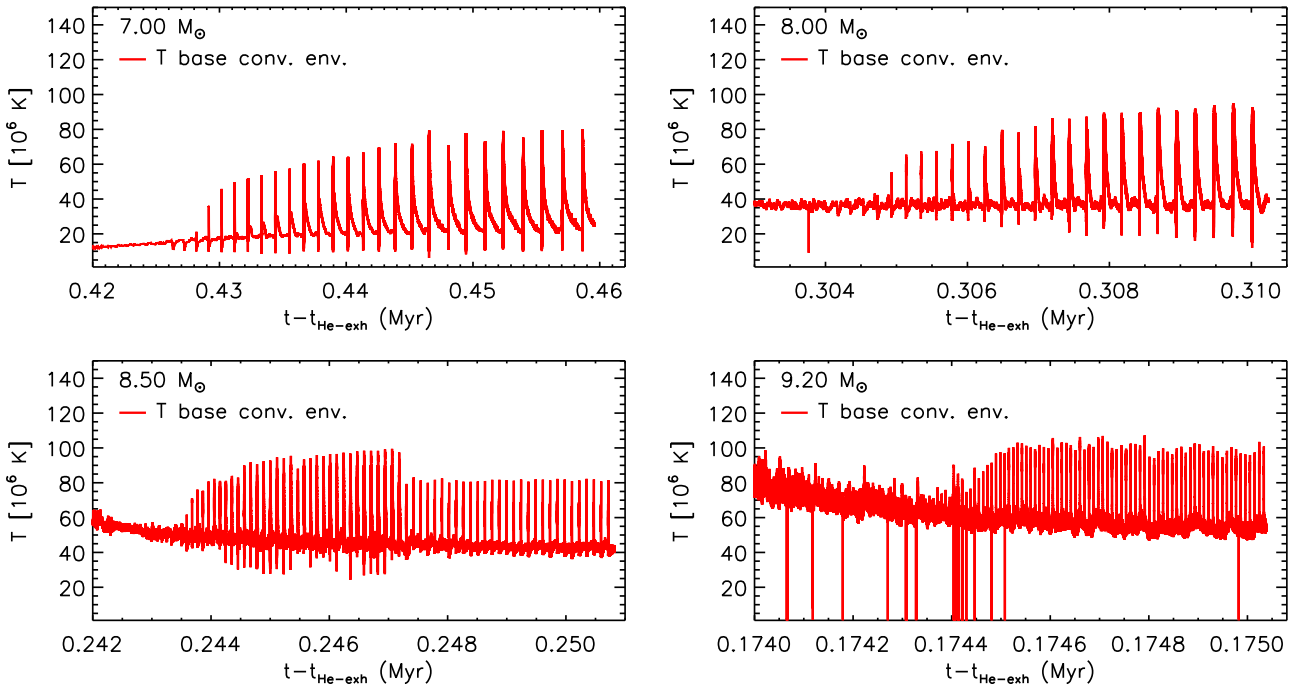

Figure 9. Evolution of the temperature at the base of the convective envelope as a function of time during the AGB phase (for the 7.0 $M_{\odot}$ model; upper left panel) and the SAGB phase (for the 8.0, 8.5, and 9.2 $M_{\odot}$ models; upper right, lower left, and lower right panels, respectively). The time has been reset at the core He exhaustion.

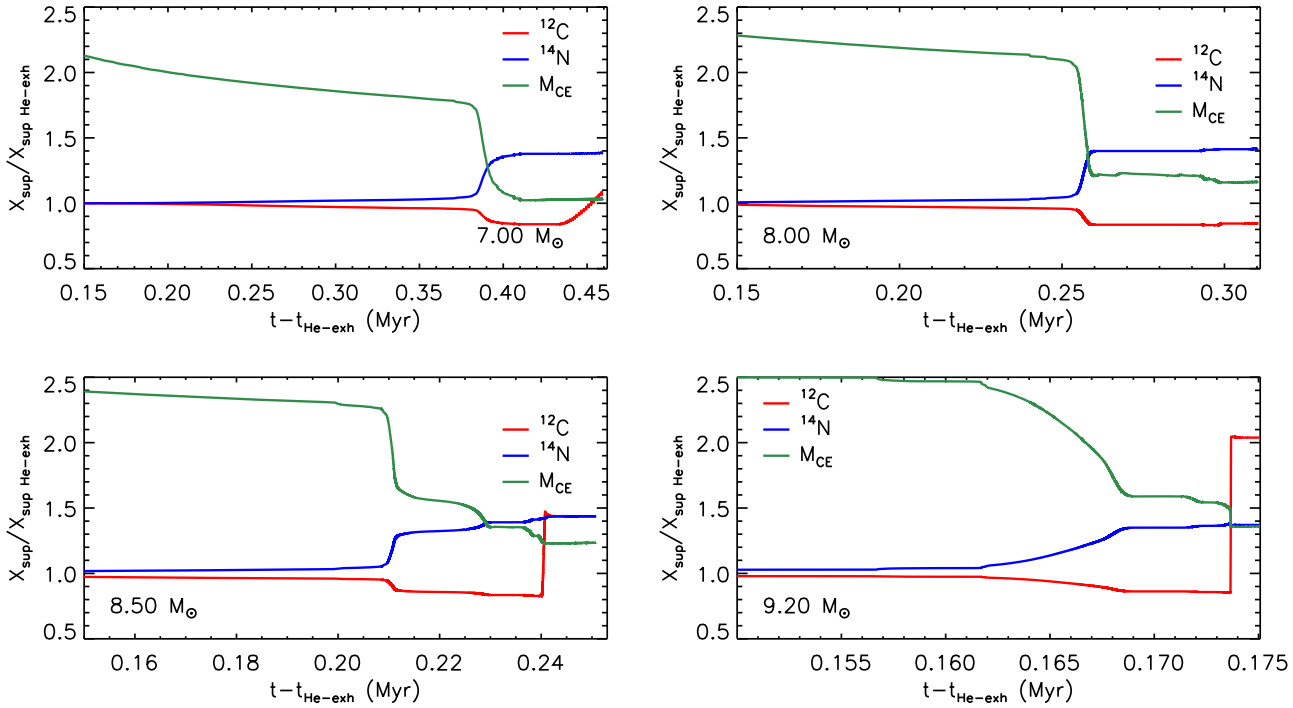

Figure 10. Evolution of the surface ^{12}C (red line) and ^{14}N (blue line) mass fraction and the mass coordinate of the bottom of the convective envelope (green line) as a function of time during the AGB phase (for the 7.0 $M_{\odot}$ model; upper left panel) and the SAGB phase (for the 8.0, 8.5, and 9.2 $M_{\odot}$ models; upper right, lower left, and lower right panels, respectively). The time has been reset at the core He exhaustion.

H-burning shell is reignited. After the convective envelope reaches its maximum depth, the H-burning shell begins to advance in mass. In this phase, the He-burning shell is progressively reignited in those stars where it was switched off. From this stage onward, for all of the stars, the evolution is characterized by a double shell burning, where the two H- and He-burning shells advance in mass with a similar rate. In fact, in this phase, the H-burning luminosity is a factor of ∼7 higher than that of the He burning (see the leftmost values in Figure 7), which corresponds roughly to the ratio between the energy provided by the CNO cycle and the energy provided by the 3α reactions. This means that the two shells burn the same